applied optics

Compressed sensing snapshot spectral imaging by a regular digital camera with an added optical diffuser

Michael A. Golub,[1,*] Amir Averbuch,[2] Menachem Nathan,[1] Valery A. Zheludev,[2] Jonathan Hauser,[1] Shay Gurevitch,[1] Roman Malinsky,[1] and Asaf Kagan[1]

[1]School of Electrical Engineering, Faculty of Engineering, Tel Aviv University, Ramat Aviv, Tel Aviv 69978, Israel
[2]School of Computer Science, Faculty of Exact Sciences, Tel Aviv University, Ramat Aviv, Tel Aviv 69978, Israel
*Corresponding author: mgolub@eng.tau.ac.il

Received 6 August 2015; revised 26 November 2015; accepted 26 November 2015; posted 30 November 2015 (Doc. ID 247375); published 11 January 2016

We propose a spectral imaging method that allows a regular digital camera to be converted into a snapshot spectral imager by equipping the camera with a dispersive diffuser and with a compressed sensing-based algorithm for digital processing. Results of optical experiments are reported.

OCIS codes: (110.4234) Multispectral and hyperspectral imaging; (170.0110) Imaging systems; (170.3010) Image reconstruction techniques; (300.6190) Spectrometers.

http://dx.doi.org/10.1364/AO.55.000432

1. INTRODUCTION

"Spectral imaging" (SI) refers to the acquisition of the three-dimensional (3D) spectral cube of spatial and spectral data of a source object at a limited number of wavelengths in a given wavelength range. SI has a multitude of applications in many fields [1], including biology [2], medicine [3–5], food inspection [6,7], archeology, art conservation [8], astronomy and remote sensing [9]. SI with mosaic spectral filter arrays on the image sensor [10] leads to substantial light gathering losses. In "staring" or "pushbroom" SI systems [11], removable sets of narrow bandpass filters [6] or time-sequential dynamic spectral filters [12] slow the SI process and cannot apply it to dynamic, fast changing objects. Modern trends in digital imaging [1] resort to a generic combination of optics with digital processing and to compressed sensing (CS) [13–25] for various purposes and applications. CS-based algorithms already have wide applications in astronomy, biology, medicine, radar, and seismology [26,27].

"Snapshot spectral imaging" (SSI) refers to the instantaneous acquisition (in a single "shot") of the spectral cube, a process suitable for fast changing objects. Recent CS applications in SSI [28–39] minimize the trade-off between spatial and spectral resolution in a snapshot imaging spectrometer. There are several known SSI devices/architectures that demonstrate the progress and high potential of SSI, including the nonscanning computed-tomography imaging spectrometer [40–43], the image replicating imaging spectrometer [44], the multispectral Sagnac interferometer [45], the multishot snapshot spectral imager [34], the snapshot image mapping spectrometer [35], and the coded aperture snapshot spectral imager (CASSI) [16–25,28–33]. In particular, the CASSI designs use an intermediate image plane and a coded aperture (a binary mask or a gray-scaled coded mask [22]) or a spatial light modulator [25]. The need for intermediate image formation optics (in addition to regular components of a digital camera) in several of the referenced devices increases the total track length, the weight, and the production costs of such SSI devices.

The feasibility of implementing SSI by means of only a single optical element added at the entrance pupil of a regular digital camera and by use of digital data processing was proven in [46]. However, even though the SSI system in [46] abolishes the need for a relay imaging system and for an intermediate image plane, its performance is restricted to a class of so-called "macropixel" objects composed of uniformly filled-in rectangles.

In order to convert a regular digital camera to a SSI camera for arbitrary objects, we resort here to (i) a more complicated diffusing and dispersing "phase-only" static optical element at the entrance pupil that replaces the prism of [46], and (ii) tailored CS methods for digital processing of the diffused and dispersed (DD) image recorded on the image sensor. Thus, this paper describes theory and experiment with a snapshot spectral imager based on a regular digital camera equipped with an optically transparent dispersive phase-only diffuser (or simply "diffuser") at the entrance pupil. The limited volume of data in the DD image acquired by a two-dimensional (2D) image sensor in a single snapshot poses a problem for the reconstruction of a 3D spectral cube. To overcome this

limitation and to enable SSI, we resort to compression of spatial data in multispectral images with the aid of CS-based reconstruction algorithms. The diffuser is designed to mix the spectral cube data spectrally and spatially and thus to enable convergence in its reconstruction by CS-based algorithms. We demonstrate the feasibility of reconstructing experimental SSI images with a relatively straightforward linear iterative process of "split Bregman iterations" (SBIs) [47,48]. This points to the possibility of modifying existing imaging systems currently implemented in smartphones and cameras to perform SSI, instead of having to design and build new SSI systems from scratch. Another advantage of our SSI design is that the suggested diffuser transmits about twice as much light as a binary amplitude coded aperture.

2. SPECTRAL IMAGING WITH A DISPERSIVE DIFFUSER

Our goal was to develop a SSI camera and SSI method based essentially on the use of a standard digital camera having a single additional optical element at the entrance pupil and on specialized digital image processing software for CS-based spectral imaging. As shown in Fig. 1, our SSI camera includes elements of a regular digital camera, such as an imaging lens, an image sensor, a bandpass spectral filter, and a digital processor, as well as the additional diffuser at the entrance pupil.

To define the diffuser design, we resorted to a combination of approaches customary in CS theory and in classical spectroscopy. To succeed in image reconstruction and to satisfy a restricted isometry property (RIP) condition [13], modern CS theory requires a highly randomized system response. Classical spectroscopic systems comprise a dispersive optical element like a prism or a diffraction grating. In order to minimize the required number of optical elements and to restrict our imager design to a modification of standard digital cameras, we decided to combine dispersive and diffusing properties required from the added optical element in a single "RIP diffuser." The RIP diffuser is positioned at the entrance pupil of the imaging lens and works as a random dispersing element that provides the DD image at the image sensor. A digital processor processes the DD image to reconstruct a plurality of monochromatic images (i.e., the spectral cube) of the source object through iterative CS-based algorithms.

Even though the RIP diffuser is physically located at the entrance pupil of the imaging lens, it is convenient in the design stage to scale the coordinates at the RIP diffuser to the size of the exit pupil by the pupil magnification coefficient. Cartesian coordinates at the RIP diffuser plane on the scale of the exit pupil are denoted as u', v'. The RIP diffuser is designed as a thin phase optical element with linear dimensions $D_{u'} \times D_{v'}$ fabricated of a transparent material and consisting of $N_d = D_{u'}/\Delta u'$ vertical straight-line strips with widths $\Delta u'$ extending parallel to the v' axis, as shown in Fig. 2. Groove depths and respective phases are constant within the width $\Delta u'$ of the kth strip and quantized to N_Q discrete phase levels that are equidistant from each other with a phase difference of $2\pi/N_Q$.

This section and others below present a set of mathematical equations as follows: first, Eqs. (1–7) describe the phase, groove depths, and the complex transmission function of the RIP diffuser. Equations (8–11) describe the response of the entire optical system with the RIP diffuser in terms of a point spread function (PSF) and a continuous convolution integral. Spatial and spectral sampling of the convolution integral, as well as analytical calculations of the PSF are presented using Eqs. (12–21). The latter enable the matrix formulation for a CS model of the optical system comprising the RIP diffuser in Eqs. (22–29). The impact of a framelet transform is described using Eqs. (30–33). The RIP condition and the CS iterative process for reconstruction of the spectral cube from the DD image are described using Eqs. (34–42). Finally, merit functions for the numerical quality of the reconstruction are described using Eqs. (43–45).

Several different design options for RIP diffusers were analyzed and their performance was compared with computer simulations. The final design choice for the RIP diffuser's phase function was a randomly permutated, nonlinear sawtooth phase. The intuitive reason for this choice is that a sawtooth diffraction grating supports spectral dispersion and that random permutation with a nonlinearity supports a random response, which is preferable for compressed sensing. The RIP diffuser provides wavelength-dependent light diffusion and accordingly serves as an inherent disperser. Therefore, it provides spectral multiplexing along with spatial multiplexing. In particular, the RIP diffuser modifies the PSF of the imaging system and renders the sensing matrix appropriate for reconstruction of the spectral cube with the aid of CS algorithms that resort to a sparse representation of the object.

Figure 3 shows the main stages of the RIP diffuser design. We started with a blazed diffraction grating having a sawtooth profile with period $\Lambda = N_Q \Delta u'$ in the u' axis direction and a periodic sawtooth phase function

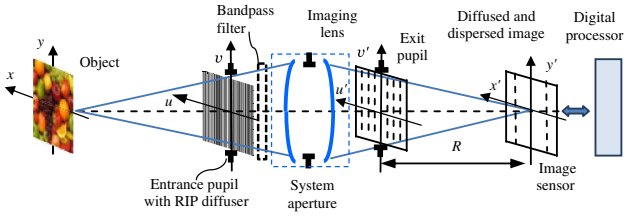

Fig. 1. Optical scheme of a spectral imaging optical system based on a digital camera and a RIP diffuser.

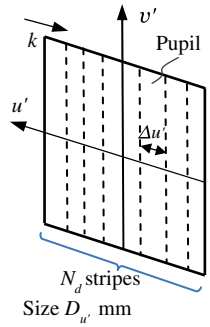

Fig. 2. Dimensions of the RIP diffuser, scaled to exit pupil coordinates.

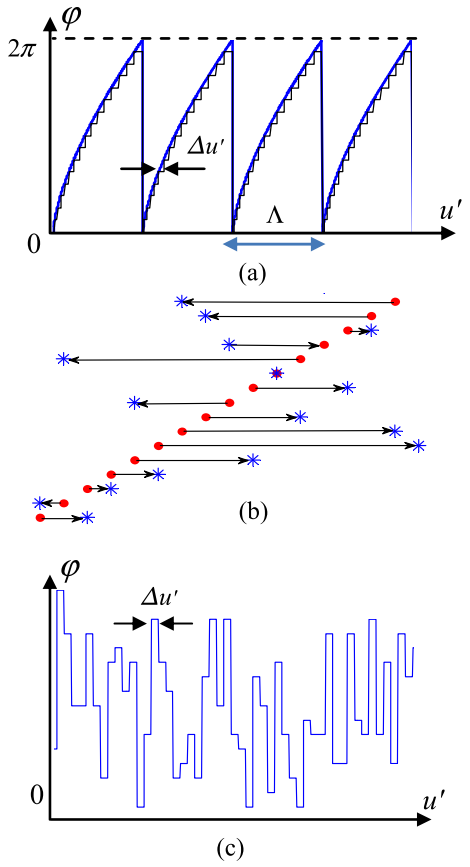

Fig. 3. Stages of RIP diffuser design: (a) nonlinear transformation of a sawtooth function and the 16-level quantization; (b) random spatial permutation of pixels; (c) fragment of a randomized piecewise-constant phase function of the RIP diffuser.

$$\varphi_{\text{sawtooth}}(u') = \text{mod}_{2\pi}\left(2\pi\frac{u'}{\Lambda}\right). \tag{1}$$

Here, $\text{mod}_{2\pi}(\cdot)$ denotes a minimum positive residue of the argument after subtracting multiples of 2π. We then executed a sampling $\varphi_{\text{sawtooth}}(u'_k)$ at middle points

$$u'_k = \left(k - \frac{N_d+1}{2}\right)\Delta u' \tag{2}$$

of the strips and applied a nonlinearity function Q, specifically chosen in our experiments as a power 2/3. Accordingly, the nonlinearly transformed phase function $\varphi_{k,\text{nonlin}}$ can be expressed by

$$\varphi_{k,\text{nonlin}} = Q[\varphi_{\text{sawtooth}}(u'_k)] = 2\pi\left[\frac{1}{2\pi}\varphi_{\text{sawtooth}}(u'_k)\right]^{\frac{2}{3}}. \tag{3}$$

Next, the design values of $\varphi_{k,\text{nonlin}}$ were quantized to N_Q equidistant discrete phase levels, as shown in Fig. 3(a). Finally, we introduced randomization by spatial permutation of the pixels $\varphi_{k,\text{nonlin}}$, as shown in Fig. 3(b). The resulting phase function of the RIP diffuser has a randomly selected phase $\varphi_{k,\text{des}}$ constant within a strip $|u' - u'_k| \le \Delta u'/2$, $k = \overline{1, N_d}$, as shown in Fig. 3(c). The groove depths are proportional to the design phase and can be calculated in the paraxial case as [49]

$$h_k = \frac{\varphi_{k,\text{des}}}{2\pi}\frac{\lambda_{\text{des}}}{n(\lambda_{\text{des}}) - 1}, \tag{4}$$

where λ_{des} is the design wavelength and $n(\lambda_{\text{des}})$ is the refractive index of the groove material.

Although the RIP diffuser was designed for wavelength λ_{des}, other wavelengths in the entire spectral range are incident on it. In fact, the spectral cube uses a finite number L of spectral bands with central wavelengths λ_l, $l = \overline{1, L}$ out of the entire continuous wavelength range. At a certain central wavelength λ_l, the groove depths h_k in Eq. (4) remain unchanged while the phase changes as [49]

$$\varphi_{k,l} = \varphi_{k,\text{des}}\frac{\lambda_{\text{des}}}{\lambda_l}\frac{n(\lambda_l) - 1}{n(\lambda_{\text{des}}) - 1} \cong \varphi_{k,\text{des}}\frac{\lambda_{\text{des}}}{\lambda_l}. \tag{5}$$

The approximation in Eq. (5) can be applied because n varies slowly compared to wavelength variations. Accordingly, the pixels

$$P_{kl} = \exp(i\varphi_{k,l}) \tag{6}$$

describe the complex transmission function $P(u', v'; \lambda_l)$ of the RIP diffuser in the SI system. The dependence on a continuous coordinate u' has a 1D piecewise constant nature, same as the phase of the RIP diffuser, and can be formally expressed as

$$P(u', v'; \lambda_l) = \sum_{k=0}^{N_d} P_{kl}\,\text{rect}\left(\frac{u' - u'_k}{\Delta u'}\right)\text{rect}\left(\frac{v'}{D_{v'}}\right), \tag{7}$$

where the value of the function $\text{rect}(\xi)$ is 1 for $|\xi| \le 0.5$ and 0 at other points. The insertion of the RIP diffuser into the optical system modifies the system pupil function by multiplication over $P(u', v'; \lambda_l)$.

When installed into the SI optical system, the RIP diffuser converts the original image into a DD image with programmed blur for each object point. We assumed that before introduction of the 1D RIP diffuser, the imaging system was spatially shift invariant and its optical resolution was matched to the sensor pixel pitch. Accordingly, the pupil function of the entire SI optical system can be approximated by $P(u', v'; \lambda_l)$. Therefore, the coherent PSF can be calculated as an inverse Fourier transform of the piecewise constant pupil function Eq. (7),

$$h(x', y'; \lambda) = \frac{1}{i\lambda R}\int P(u', v'; \lambda)\exp\left(i2\pi\frac{u'x' + v'y'}{\lambda R}\right)\text{d}u'\text{d}v'$$
$$= h(x'; \lambda)\text{sinc}\left(\frac{D_{v'}}{\lambda R}y'\right), \tag{8}$$

where

$$h(x'; \lambda) = \frac{D_{u'}D_{v'}}{i\lambda R}\,\text{sinc}\left(\frac{\Delta u'}{\lambda R}x'\right)\frac{1}{N_d}\sum_{k=0}^{N_d} P_{kl}\,\exp\left(i2\pi u'_k\frac{x'}{\lambda R}\right), \tag{9}$$

is the 1D version of $h(x', y'; \lambda)$, R is the distance from the center of the exit pupil to the image sensor, and $\text{sinc}(\xi) = \frac{\sin(\pi\xi)}{\pi\xi}$. Accordingly, the 1D incoherent PSF associated with the RIP diffuser at wavelength λ_l is

$$h_I(x'; \lambda_l) = |h(x'; \lambda_l)|^2. \tag{10}$$

The intensity $I'(x', y; \lambda_l)$ of the DD image in the presence of the RIP diffuser may be expressed by just a 1D convolution

$I' = h_I \otimes I$ of the ideal ("nondispersed") image $I(x, y; \lambda_l)$ with the incoherent PSF $h_I(x'; \lambda_l)$. The convolution is calculated separately for each coordinate y of the object as

$$I'(x', y; \lambda_l) = \int h_I(x' - x; \lambda_l) I(x, y; \lambda_l) \mathrm{d}x. \tag{11}$$

3. COMPRESSED SENSING MODEL FOR SPECTRAL IMAGING

The CS theory [13–15,26,27,36–39,47,48,50–53] provides a method to capture and represent compressible images at a rate significantly below the Nyquist rate by exploiting the sparse nature of the image data in some mathematical basis. This may be done using nonadaptive linear projections that enable the full reconstruction of the spectral cube of the source object. The full reconstruction can be performed using an iterative optimization process to compensate for the underdetermined nature of the problem. The operator performing the linear projections can be described by a "sensing matrix" that has fewer rows than columns and which operates on the spectral cube to form the DD image.

Application of the CS approach to the SSI camera shown in Fig. 1 requires a transfer from continuous coordinates of optics to discrete indices of CS vectors and sensing matrix. To start, we consider the discrete pixelated structure of the image sensor, which is characterized along the x and y axes by a 2D spatial pitch $\delta_x \times \delta_y$, a number N_x, N_y of pixels, and a number N_b of bits per pixel. The imaging zoom has to match the blur caused by the PSF of the RIP diffuser such that the entire DD image stays within the aperture of the image sensor, i.e., within N_x pixels in each row and N_y pixels in each column. The "nondiffused-nondispersed" image obtained without a RIP diffuser at same zoom is spread to a lesser degree, and occupies accordingly only a smaller number $N < N_x$ of pixels located in the central part of each image sensor row. Even though the number $N_x \times N_y$ of sensed pixels may be smaller than the number of voxels $N \times N_y \times L$ in the targeted 3D spectral cube, the CS approach is supposed to enable restoration of the entire spectral cube with reasonable accuracy. This is a result of the well-known redundancy in image data, which allows for a compressed representation of an image. In our notations, the data compression rate is $N \times L/N_x$.

To proceed with discrete notations customary in compressed sensing, we define index ranges. Figure 4 shows ranges $i = \overline{1, N}$ and $i' = \overline{1, N_x}$ that run in the x direction of the spectral cube and of the image sensor, respectively. We denote the shift of one range to the other by

$$i_c = \frac{N_x - N}{2} > 0. \tag{12}$$

Indices $j' = j = \overline{1, N_y}$ run in the y direction of the spectral cube and the sensor, and range $l = \overline{1, L}$ corresponds to the wavelength direction of the spectral cube. The image sensor pixel centers have the Cartesian coordinates

$$x_{i'} = \left(i' - \frac{N_x + 1}{2}\right)\delta_x, \qquad y_{j'} = -\left(j' - \frac{N_y + 1}{2}\right)\delta_y. \tag{13}$$

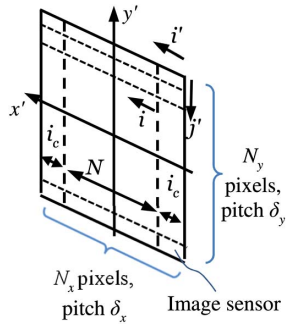

Fig. 4. Dimensions for the diffused and dispersed image on the image sensor.

Accordingly, the Cartesian spatial coordinates for the spectral cube are x_{i+i_c} and $y_{j'}$. Now, sampling of coordinates at each wavelength in the PSF of Eqs. (9) and (10) provides a Toeplitz convolution kernel,

$$h_I(x_{i'} - x_{i+i_c}; \lambda_l) = \left(\frac{D_{u'} D_{v'}}{\lambda_l R}\right)^2 K_{i'-i,l}, \tag{14}$$

where $\Delta i' = i' - i$, $i = \overline{1, N}$, $i' = \overline{1, N_x}$, $l = \overline{1, L}$,

$$K_{\Delta i', l} = \mathrm{sinc}^2\left(\frac{\Delta i' - i_c}{N_l}\right)\frac{1}{N_d^2} \times \left|\sum_{k=0}^{N_d} P_{kl} \exp\left[i\frac{2\pi}{N_l}\left(k - \frac{N_d + 1}{2}\right)(\Delta i' - i_c)\right]\right|^2, \tag{15}$$

$$N_l = \frac{\lambda_l R}{\Delta u' \delta_x}, \tag{16}$$

and P_{kl} is defined by Eqs. (5) and (6). Note that array $K_{\Delta i', l}$ for fixed $l = \overline{1, L}$ has a range $\Delta i' = \overline{-(N - 1), (N_x - 1)}$ and therefore includes $N_x + N - 1$ elements.

A discrete version of the spectral cube in each spectral band can be expressed by the $N \times N_y \times L$ matrix,

$$\mathbf{X} = (X_{i,l}^{(j)}, i = \overline{1, N}, j = \overline{1, N_y}), \tag{17}$$

where spectral cube voxels can be expressed as

$$X_{i,l}^{(j)} = I(x_{i+i_c}, y_j; \lambda_l), \qquad i = \overline{1, N}, \qquad j = \overline{1, N_y}, \qquad l = \overline{1, L}. \tag{18}$$

The continuous 1D convolution in Eq. (11) is converted into a discrete convolution applied separately to each of N_y image rows. Due to Eqs. (9) and (14), discrete pixels of the DD image at the l_{th} wavelength and at a given j can be expressed as a discrete 1D aperiodic convolution,

$$I'(x_{i'}, y_j; \lambda_l) = \left(\frac{D_{u'} D_{v'}}{\lambda_l R}\right)^2 \delta_x \sum_{i=1}^{N} K_{i'-i,l} X_{i,j,l}, \tag{19}$$

where $i' = \overline{1, N_x}$, $j = \overline{1, N_y}$, $l = \overline{1, L}$. Note that in our model with a 1D RIP diffuser, each $j' = j^{\text{th}}$ row of the DD image is in one-to-one correspondence with a respective j^{th} row of the spectral cube.

The contribution of polychromatic light to discrete pixels of the DD image is denoted as $Y_{i'}^{(j)}$ and can be expressed as a sum of the intensities of monochromatic DD images $I'(x_{i'}, y_j; \lambda_l)$ over all wavelengths λ_l, $l = \overline{1, L}$. At each image pixel, the sum can be expressed as

$$Y_{i'}^{(j)} = \frac{1}{\delta_x} \sum_{l=1}^{L} \left(\frac{\lambda_l R}{D_{u'} D_{v'}} \right)^2 \kappa_l I'(x_{i'}, y_j; \lambda_l) = \sum_{l=1}^{L} \sum_{i=1}^{N} A_{i',i,l}^{(j)} X_{i,l}^{(j)}, \tag{20}$$

where nonnegative numbers κ_l characterize the overall relative spectral sensitivity of the image sensor and the optical transmission of the optical components of the system at wavelength λ_l, and where coefficients

$$A_{i',i,l}^{(j)} = \kappa_l K_{i'-i,l}, \qquad i = \overline{1, N}, \qquad i' = \overline{1, N_x}, \qquad l = \overline{1, L}, \qquad j = \overline{1, N_y} \tag{21}$$

describe the effect of the RIP diffuser scaled with the relative spectral sensitivity of the optical system.

For mathematical considerations, it is convenient to concatenate spectral and vertical spatial dimensions of the spectral cube, i.e., to substitute two indices i, l by a single index in arrays $X_{i,l}^{(j)}$ and $A_{i',i,l}^{(j)}$. Accordingly, we resort to a 1D vector $\mathbf{X}^{(j)} = (X_{i,l}^{(j)}, i = \overline{1, N}, l = \overline{1, L})$ with enlarged length NL:

$$\mathbf{X}^{(j)} = \begin{pmatrix} X_{1,j,1} \\ \vdots \\ X_{N,j,1} \end{pmatrix} \lambda_1 \\ \vdots \\ \begin{pmatrix} X_{1,j,L} \\ \vdots \\ X_{N,j,L} \end{pmatrix} \lambda_L, \qquad j = \overline{1, N_y}. \tag{22}$$

The entire set of N_y vectors $\mathbf{X}^{(j)}$, $j = \overline{1, N_y}$ can be merged into a matrix,

$$\mathbf{X} = [\mathbf{X}^{(j)}, j = \overline{1, N_y}] = [\mathbf{X}^{(1)}, \mathbf{X}^{(2)}, \ldots, \mathbf{X}^{(N_y)}], \tag{23}$$

of size $NL \times N_y$ that includes the entire spectral cube data. Matrix $\mathbf{X}$ can alternatively be split into L spectral dimensions,

$$\mathbf{X} = \begin{bmatrix} \mathbf{X}_1 \\ \mathbf{X}_2 \\ \vdots \\ \mathbf{X}_L \end{bmatrix}, \tag{24}$$

such that each spectral dimension is described by a submatrix $\mathbf{X}_l$ of size $N \times N_y$, as shown in Fig. 5. We define a $N_x \times NL$ dimensional block Toeplitz sensing matrix,

$$A = (A_{i',i,l}, i' = \overline{1, N_x}, i = \overline{1, N}, l = \overline{1, L}), \tag{25}$$

which may be treated as a block rectangular matrix, $A = [A_1, A_2, \ldots A_L]$, composed of L Toeplitz submatrices A_l of size $N_x \times N$ each. Each submatrix A_l corresponds to a single wavelength and features the randomization originating from the RIP diffuser. We also define a single column vector of the multiple-column 2D DD image,

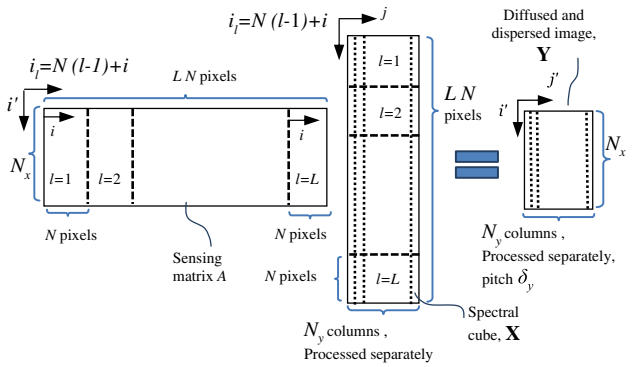

Fig. 5. Transformation of the spectral cube to the dispersed-diffused image by the sensing matrix.

$$\mathbf{Y}^{(j)} = (Y_{i'}^{(j)}, i' = \overline{1, N_x}) = \begin{pmatrix} Y_1^{(j)} \\ \vdots \\ Y_{N_x}^{(j)} \end{pmatrix}, \qquad j = \overline{1, N_y}, \tag{26}$$

with components determined in Eq. (20). The entire set of N_y vectors $\mathbf{Y}^{(j)}, j = \overline{1, N_y}$ can be merged into a matrix of size $N_x \times N_y$ representing the DD image:

$$\mathbf{Y} = [\mathbf{Y}^{(j)}, j = \overline{1, N_y}] = [\mathbf{Y}^{(1)}, \mathbf{Y}^{(2)}, \ldots, \mathbf{Y}^{(N_y)}]. \tag{27}$$

Note that $\mathbf{X}^{(j)}$ is a single column vector from the spectral cube to be reconstructed from the single column sensed vector $\mathbf{Y}^{(j)}$. Matrix $\mathbf{X}$ represents the spectral data to be reconstructed from DD image $\mathbf{Y}$.

Equation (20) can now be expressed in matrix form as the multiplication of a vector of length NL over a matrix of size $N_x \times NL$. The multiplication results in a vector of a smaller length N_x:

$$\mathbf{Y}^{(j)} = A\mathbf{X}^{(j)}. \tag{28}$$

For efficient 2D data processing, Eq. (28) can be expressed in matrix form as the multiplication of matrix $\mathbf{X}$ of size $NL \times N_y$ over the sensing matrix A of size $N_x \times NL$, resulting in a matrix of smaller size $N_x \times N_y$,

$$A\mathbf{X} = \mathbf{Y}, \tag{29}$$

as customary in CS theory.

Equation (29) provides the CS model for our spectral imaging system. It shows that the recorded DD image $\mathbf{Y}$ includes a linear mixture of spectral and spatial data of the entire spectral cube $\mathbf{X}$, as described by sensing matrix A. The CS problem consists of the reconstruction of matrix $\mathbf{X}$ in such a way that Eq. (29) with a given matrix $\mathbf{Y}$ becomes satisfied. The number $N_x \times N_y$ of equations for $\mathbf{Y}$ in Eq. (29) is less than the number of unknown variables $NL \times N_y$ in $\mathbf{X}$. Accordingly, the reconstruction problem seems to be ill-posed and as such has an infinite number of solutions, of which, however, some do not have any physical sense.

To obtain a sensible solution, we have to impose some constraints on the spectral cube to be reconstructed. The commonly chosen constraint in CS is sparsity. The latter originates from a well-established fact that 2D digital images

have a sparse representation in wavelet and wavelet-frame domains. Consequently, spectral cubes, which are collections of monochromatic images, possess the same property, i.e., they can be represented as collections of sparse matrices that contain many zeroes. Therefore, in accordance with the CS theory, we look for a solution of Eq. (29) that is maximally sparse in a wavelet-frame domain.

The mathematical relation between spectral cube matrix $\mathbf{X}$ and its sparse representation $\mathbf{d}$ (having only a relatively small number of nonzero elements) can be represented as a linear transform $\mathbf{d} = D\mathbf{X}$, with a "sparsifying" matrix D. The sparse representation may be implemented by resorting to 2D framelet transforms, described in detail in [14]. In particular, a detailed description of the design of a variety of frames-generating filter banks based on polynomial and discrete splines is given in [14,54]. In our spectral image reconstruction experiments we used 2D semi-tight frame transforms. Direct and inverse transforms were implemented by application of analysis and synthesis of four-channel filter banks with down- (up)-sampling factor 2. Each filter bank comprises one low-pass, one high-pass, and two bandpass filters. "Semi-tightness" means that the low-pass and high-pass filters are the same for the analysis and the synthesis filter banks, but that the bandpass filters are different. The filters originate from the quasi-interpolating quadratic splines and have finite impulse responses and linear phases. It was shown in [14,54] that wavelet frames are more advantageous than wavelets, because they demonstrate better adaptivity to specific images due to redundant representation of images. Sparsity of an image in the wavelet-frame domain means that the image can be represented with sufficient accuracy by a linear combination of a relatively small number of framelets. This number is significantly less than the number of pixels in the image.

We apply a direct 2D linear framelet transform separately to each submatrix $\mathbf{X}_l$, $l = 1, \ldots, L$, of matrix $\mathbf{X}$. The transform can be presented as the multiplication of the submatrices $\mathbf{X}_l$ over sparsifying matrix D. This operation maps matrix $\mathbf{X}$ onto a blockwise sparse matrix $\mathbf{d}$ consisting of framelet transform coefficients, such that

$$\mathbf{d} = D\mathbf{X} \Leftrightarrow \begin{pmatrix} D\mathbf{X}_1 \\ D\mathbf{X}_2 \\ \vdots \\ D\mathbf{X}_L \end{pmatrix} = \begin{pmatrix} \mathbf{d}_1 \\ \mathbf{d}_2 \\ \vdots \\ \mathbf{d}_L \end{pmatrix}, \tag{30}$$

where $\mathbf{d}_l$, $l = 1, \ldots, L$, are submatrices of $\mathbf{d}$, i.e., matrices having only a relatively small number of nonzero elements. We denote by Ψ the matrix of the inverse 2D linear frame transform, such that spectral cube $\mathbf{X}$ can be restored from its K-sparse representation $\mathbf{d}$ by

$$\mathbf{X} = \Psi\mathbf{d} \Leftrightarrow \begin{pmatrix} \Psi\mathbf{d}_1 \\ \Psi\mathbf{d}_2 \\ \vdots \\ \Psi\mathbf{d}_L \end{pmatrix} = \begin{pmatrix} \mathbf{X}_1 \\ \mathbf{X}_2 \\ \vdots \\ \mathbf{X}_L \end{pmatrix}. \tag{31}$$

Now Eq. (29) can be expressed in the form

$$\Theta\mathbf{d} = \mathbf{Y}, \tag{32}$$

where

$$\Theta = A\Psi. \tag{33}$$

The CS theory [13] addresses the feasibility for reconstruction of the sensible solution of Eq. (32) for a special case of K-sparse matrices or vectors $\mathbf{d}$ that have only K nonzero elements with known locations. It is known that the K-sparse sensible solution $\mathbf{d}$ of Eq. (32) [and consequently $\mathbf{X}$ of Eq. (29)] exists and can be reconstructed for a class of matrices Θ that satisfy a RIP condition of order K. The RIP condition of order K in CS [13] demands that any submatrix of Θ formed by less than K columns must satisfy the inequality,

$$(1 - \delta_K)\|\mathbf{d}\|_{l_2} \le \|\Theta\mathbf{d}\|_{l_2} \le (1 + \delta_K)\|\mathbf{d}\|_{l_2}, \tag{34}$$

for any K-sparse vector $\mathbf{d}$, where $\delta_K > 0$ is some small number and where the l_2 norm of a vector $\mathbf{d}$ is

$$\|\mathbf{d}\|_{l_2} = \left\{ \sum\nolimits_{i,j} |d_{i,j}|^2 \right\}^{\frac{1}{2}}. \tag{35}$$

An example of a sensing matrix satisfying the RIP condition with high probability is a random matrix [15,50] or a random Toeplitz matrix [51] formed by Gaussian random variables with zero mean value and $1/NL$ variance.

For CS-based reconstruction of sparse representation $\mathbf{d}$ of spectral cube $\mathbf{X}$ from DD image $\mathbf{Y}$, we resorted to split Bregman iterations [47,48]. Specifically, $\mathbf{d}$ was reconstructed as a solution of the following constrained minimization problem: find

$$\min_{\mathbf{d}} \|\mathbf{d}\|_{l_1} \quad \text{with conditions:} \|A\mathbf{X} - \mathbf{Y}\|_{l_2} \le \sigma, \quad \mathbf{d} = D\mathbf{X}. \tag{36}$$

Here, the l_2 norm of a matrix $\mathbf{M} = \{M_{i,j}\}$ is defined in Eq. (35) and the l_1 norm is

$$\|\mathrm{M}\|_{l_1} = \sum_{i,j} |M_{i,j}|. \tag{37}$$

The minimization problem may be formally treated as equivalent to minimization of a functional:

$$\|\mathbf{d}\|_{l_1} + \frac{\mu}{2}\|A\mathbf{X} - \mathbf{Y}\|_{l_2}^2 + \frac{\chi}{2}\|\mathbf{d} - D\mathbf{X}\|_{l_2}^2. \tag{38}$$

where μ, χ are Lagrange weight coefficients. Following [55], a closed loop of the iterative algorithm uses a feedback from the l_1 error and a shrinking operation that ensures a sparse reconstruction. In more detail, the minimization of functional Eq. (38) is performed by an iterative process,

$$\begin{cases} \mathbf{X}^{k+1} = (\mu A^T A + \chi I)^{-1}[\mu A^T(-\mathbf{c}^k) + \chi D^T(\mathbf{d}^k - \mathbf{b}^k)] \\ \mathbf{d}^{k+1} = \mathrm{shrink}\left(D\mathbf{X}^{k+1} + \mathbf{b}^k, \frac{1}{\chi}\right) \\ \mathbf{b}^{k+1} = \mathbf{b}^k + \delta_b(D\mathbf{X}^{k+1} - \mathbf{d}^{k+1}) \\ \mathbf{c}^{k+1} = \mathbf{c}^k + \delta_c(A\mathbf{X}^{k+1} - \mathbf{Y}), \end{cases} \tag{39}$$

where k is the number of the iteration, $\mathbf{b}^k$ and $\mathbf{c}^k$ are intermediate vectors used to execute iterations, A^T denotes a transposed matrix A, $\delta_b = 1$, $\delta_c = 1$, and

$$\mathrm{shrink}(x, \gamma) = \mathrm{sgn}(x)\max(|x| - \gamma, 0) \tag{40}$$

is the function applied to each vector component. The shrink function eliminates components with magnitudes not

exceeding a threshold γ and shrinks the remaining components. The shrinkage operation provides the new value for vector $\mathbf{d}$ at each iteration. The parameters of the process μ, χ (where χ^{-1} is a shrinkage threshold) give proper weights to the terms in the functional, Eq. (38), to enable convergence to a sensible solution. In particular, coefficient χ weights the sparsity level of $\mathbf{d}$, and coefficient μ weights the fit of $A\mathbf{X}$ to $\mathbf{Y}$. The reconstruction process using sensing matrix A defined in Eqs. (21) and (25) guarantees a satisfactory reconstruction of the source object, in a case where the sensing matrix satisfies the RIP condition expressed in Eq. (34). The iterations are terminated once the inequality $\|A\mathbf{X}^{k+1} - \mathbf{Y}\|_{l_2} \le \sigma$ is achieved, where σ is a stopping threshold dependent on a noise level in DD image $\mathbf{Y}$.

After completion of the iterations, we obtain the compressible blockwise matrix for reconstructed data cube $\mathbf{X}$, with components $X_{i,l}^{(j)}$ arranged as a set of vectors with spectral data for every spatial pixel. Reordering of the components provides a reconstructed submatrix,

$$\mathbf{X}_l = \begin{pmatrix} X_{1,l}^{(1)} & \cdots & X_{1,l}^{(N_y)} \\ \vdots & \vdots & \\ X_{N,l}^{(1)} & \cdots & X_{N,l}^{(N_y)} \end{pmatrix}, \tag{41}$$

of size $N \times N_y$ in each spectral band λ_l, where $l = \overline{1, L}$ is the index of the corresponding spectral band. Accordingly, the intensity of the voxels of the spectral cube is found to be

$$I(x_{i+i_c}, y_j; \lambda_l) = X_{i,l}^{(j)}. \tag{42}$$

4. EXPERIMENTAL OPTICAL ARRANGEMENT AND CALIBRATION

The concept of our CS-based SSI camera was proven for $L = 33$ wavelength bands in an optical experiment that used a regular digital camera equipped with a monochromatic (without color filters matrix) image sensor, a RIP diffuser, and specialized digital image processing capabilities, as shown in Fig. 1. A color iPad screen served as the object. The experimental arrangement included the following optical components: a regular digital camera with a 5Mpixel, 12-bit Aptina Demo kit [56] monochromatic image sensor, a DSL935 Sunex imaging lens with a numerical aperture value of approximately 0.17, and a wide bandpass spectral filter for the entire visible range. The image sensor had 2592×1944 pixels with a pixel pitch $\delta_x = \delta_y = 2.20$ μm. Even though our generic hardware and software enable large dimensions, we actually used $N_y = 256$ rows and displayed only $N_x = 512$ columns for the DD image at the image sensor, which was enough to include the spread introduced by the RIP diffuser to the spectral cube with dimensions $N = 256 \times N_y = 256 \times L = 33$ pixels. The choice of the external pupil DSL935 Sunex imaging lens, whose entrance pupil is located at the first optical surface of its first lens, enabled proper placing of the RIP diffuser at this pupil. An entrance pupil diameter of 3.2 mm, an exit pupil diameter of $D_{u'} = D_{v'} = 6.5$ mm, and a location at R = 19.6 mm in front of the image plane yields an entrance-to-exit pupil magnification of 2.03.

Various RIP diffusers were fabricated at the Tel Aviv University Nano-Center facilities with a standard 16-depth level binary staircase technology on a 0.5 mm thick, double-side polished 4 in. fused silica wafer. Four photolithography stages using a set of four chrome masks were followed by reactive ion etching processes. The wafer merged 16 different RIP diffuser designs. Individual 11 mm^2 diffusers were separated after fabrication by blade-cutting. The actual RIP diffuser design used in our experiments had a 3.2 mm clear aperture that matched the entrance pupil and included $N_d = 400$, $\Delta u = 8$ μm wide stripes, as shown in Fig. 6. A special aluminum holder was used to place and conveniently exchange diffusers at the entrance pupil.

Even though Eq. (14) provides a good theoretical model for the PSF with the RIP diffuser, we performed direct calibration of the SSI camera by direct PSF measurements that provided the sensing matrix. An object with a single thin white vertical column displayed on the iPad screen was imaged in the dark at several spatial positions in each spectral band. Separated spectral bands for the calibration were achieved by resorting to a set of $L = 33$ Thorlabs narrow-bandpass 10 nm FWHM spectral filters that covered the 400–720 nm wavelength range in equal gaps of 10 nm and which were mechanically integrated in filter wheels.

We first observed that the PSF showed a negligible space-variance from the center to the periphery of the field of view, i.e., showed spatial shift invariance with respect to both the horizontal x position of the white column and the vertical y position within the column. Accordingly, we measured the PSF at a few exemplary positions. The sensor's integration time was adjusted at each spectral band to keep the peak intensity below 90% of the saturation intensity level. We then subtracted the dark image from measurements and averaged the results for several x, y positions to yield the PSF as a row vector per each spectral band. The PSF was also normalized, centered, padded

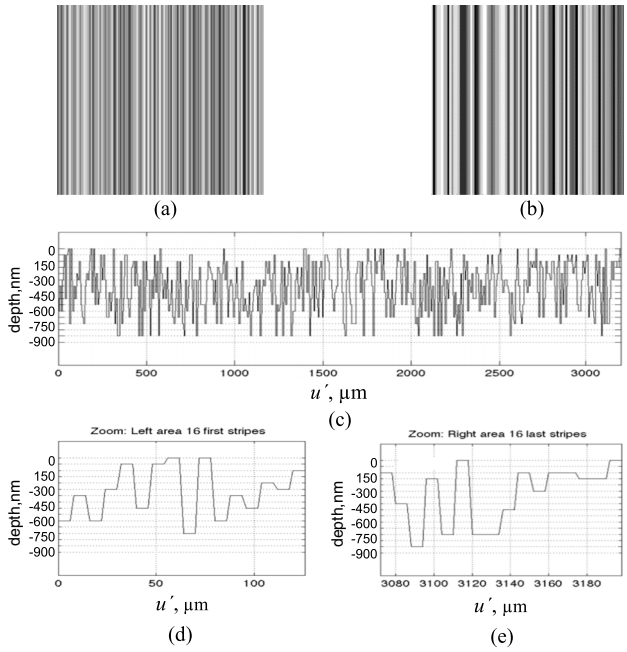

Fig. 6. RIP diffuser design: (a) gray-level map, (b) magnified fragment, (c) full profile scan, (d) left edge, (e) right edge.

Fig. 7. Illustration for the integration of the PSF into the sensing matrix A.

with zeroes, and integrated into the block Toeplitz sensing matrix A, as explained in Fig. 7. Figure 8 shows the optically measured sensing matrix, consisting of 33 blocks matching the wavelengths. We notice that the measured sensing matrix and subsequent reconstructed spectra are related to equally spaced central wavelengths of the set of $L = 33$ narrow-bandpass filters.

To have a firm reference for spectral cube reconstruction in our experiments, we conducted direct reference measurements of the spectral cube for each object of interest. Spatial alignment marks were added to the objects in order to support further processing. The measurements were performed without the RIP diffuser, by resorting to the set of 33 filters. The image sensor integration time was set to 90% of the saturation level with respect to a spectral band providing highest maximal intensity. Data processing was performed with a Matlab code whose functions were to acquire the monochromatic images, subtract dark field images, crop the original image to $N \times N_y = 256 \times 256$ pixels, and compose a $256 \times 256 \times 33$ sized matrix of a data cube.

5. OPTICAL EXPERIMENT FOR SPECTRAL IMAGING

Three exemplary test objects were used for optical SSI experiments: "mandrill," "peppers," and "color checker." These were created on the iPad screen mounted on the optical bench in the arrangement of Fig. 1, at a fixed distance of 83 cm in front of the imaging lens. The reference spectral cube measurements, the PSF measurements, and the gray-scale snapshots of the DD images were recorded on the image sensor in the dark,

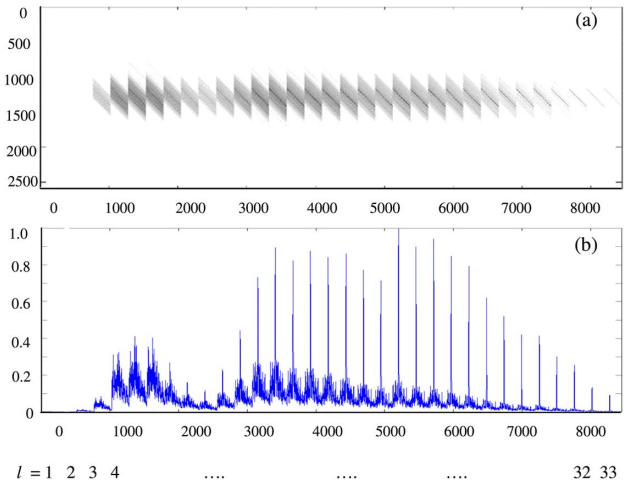

Fig. 8. Sensing matrix, built on the base of the calibration measurements: (a) gray-level plot, (b) cross section at a central row #1296.

with the RIP diffuser in place. The digital data processing started with application of a noise filter [29]. The digital reconstruction of the spectral cube was performed using the SBI process with a measured sensing matrix A and optimized iteration parameters μ, χ, as described in Section 3. The framelet transform that gave the best results was based on framelets originating from the quadratic, quasi-interpolating spline, marked in [14] as T_4^4.

Evaluation of the quality of the reconstructed spectral cubes $\mathbf{X} = (X_{i,l}^{(j)})$ was done by comparison to reference spectral cubes $\bar{\mathbf{X}} = (\bar{X}_{i,l}^{(j)})$ measured directly with the set of $L = 33$ bandpass filters. As the monochromatic images comprising the reference signal and the reconstructed spectral cubes are of the same size but do not necessarily share the same dynamic range, we normalized each to have a maximum value 1.0, separately at each spectral band. Specifically, before calculations, each of the reference and reconstructed monochromatic images in each spectral band were normalized to their individual maximal values

$$\bar{X}_{\max,l}^{(j)} = \max_{i,j} \bar{X}_{i,l}^{(j)}, \qquad X_{\max,l}^{(j)} = \max_{i,j} X_{i,l}^{(j)}. \tag{43}$$

Accordingly, we expressed the normalized root-mean-square errors (RMSE) in each spectral band as

$$\mathrm{RMSE}_l = \left\{ \frac{1}{NN_y} \sum_{i=1}^{N} \sum_{j=1}^{N_y} \left[\frac{X_{i,l}^{(j)}}{X_{\max,l}} - \frac{\bar{X}_{i,l}^{(j)}}{\bar{X}_{\max,l}} \right]^2 \right\}^{\frac{1}{2}}, \tag{44}$$

and calculated the peak signal-to-noise ratio (PSNR) as

$$\mathrm{PSNR}_l = -20 \log_{10}(\mathrm{RMSE}_l). \tag{45}$$

In addition, we resorted to visual comparison of monochromatic images at each wavelength band and comparison of spectra at chosen spatial locations. For visualization purposes, the reference and reconstructed spectral cubes were converted into RGB color images and compared to each other. The conversion was done in accordance with the CIE standard observer color matching functions implemented by Matlab function "RGB_from_Spectral_cube" taken from [57].

Figure 9 shows RGB images calculated from different spectral cubes of the "mandrill" object. Figure 9(a) shows the original object displayed on the iPad, Fig. 9(b) shows the RGB image calculated from direct measurements with the 33 bandpass filters, and Fig. 9(c) shows the DD image recorded at the image sensor with 16.0 ms integration time. Note that this time is substantially smaller than the $58.4 \times 33 = 1926$ ms needed for use of 33 bandpass filters. Such small integration time provides one major advantage of SSI over time-sequential acquisition methods. Figure 9(d) shows the RGB image built from the SBI-reconstructed spectral cube. Figure 9(e) shows the RGB image calculated from the reconstructed and noise-filtered (with an algorithm from [58]) spectral cube, which demonstrates reasonable visual quality. We emphasize that the RGB image was obtained with a monochromatic image sensor in a camera equipped with a fully transparent RIP diffuser. The rainbow patterns in Figs. 9(d) and 9(e) are likely artifacts caused by the mismatch between the mathematical model of the sensing matrix and the physical sensing matrix of the optical system with the RIP diffuser.

Figure 10 shows five out of 33 monochromatic images extracted from the spectral cubes at wavelengths 450, 540, 570,

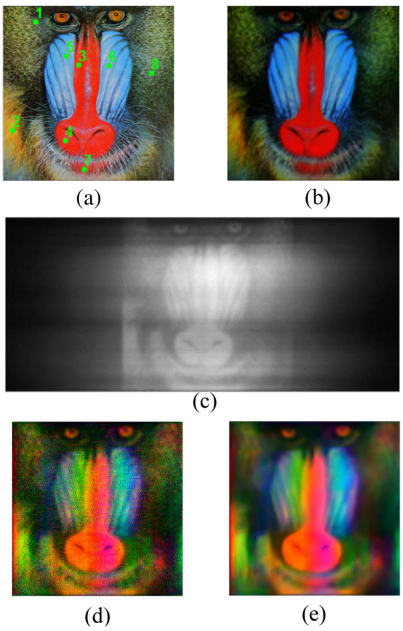

Fig. 9. Object "mandrill" with the 33 spectral bands in a range of 400–720 nm: (a) object, (b) reference directly measured with 33 spectral filters and converted to the RGB, (c) dispersed and diffused image optically recorded at the image sensor, (d) reconstructed with CS SI approach and converted to RGB format, (e) noise-filtered after reconstruction before converting to RGB.

610, and 650 nm. Figure 10(a) shows the original and Fig. 10(b) shows the filtered reconstructed images after 20 split Bregman iterations. The calculated PSNR_l (RMSE_l in brackets) values for the filtered monochromatic images at the five wavelengths are 14.64 (0.19), 14.97 (0.18), 11.82 (0.26), 20.15 (0.098), and 16.03 (0.16), respectively. Figure 10(c) shows the PSNR_l values per wavelength, while Fig. 10(d) shows the RMSE_l values per wavelength, for filtered monochromatic images CS-reconstructed from the experimental DD image (blue) and from the computer-simulated DD image (dashed black). Finally, Fig. 11 shows nonfiltered spectra at eight spatial sampling points, marked by the same numbers as in Fig. 9(a). Comparison between the reference spectra (red lines) and reconstructed experimental spectra (blue lines) for 33 spectral bands shows that critical parts of the spectrum were satisfactorily captured by our SSI optical system and digitally reconstructed. Some shifts and missing peaks in the spectra could be caused by the mismatch between the calibrated measured sensing matrix and the actual physical sensing matrix of the optical system with the RIP diffuser.

To show results that are less dependent on calibration and to demonstrate the optimal performance of our SSI camera, we resorted to the reference spectral cube and the measured sensing matrix and ran computer simulations for the DD image that would be created on the image sensor according to Eq. (29). We then derived a spectral cube reconstructed from the computer-simulated DD image. The dashed black curves in Fig. 11 show the computer-simulated spectra, which are better fitted to the reference spectra than the spectra reconstructed from the optical experiment. Specifically, the RMSE errors of the blue

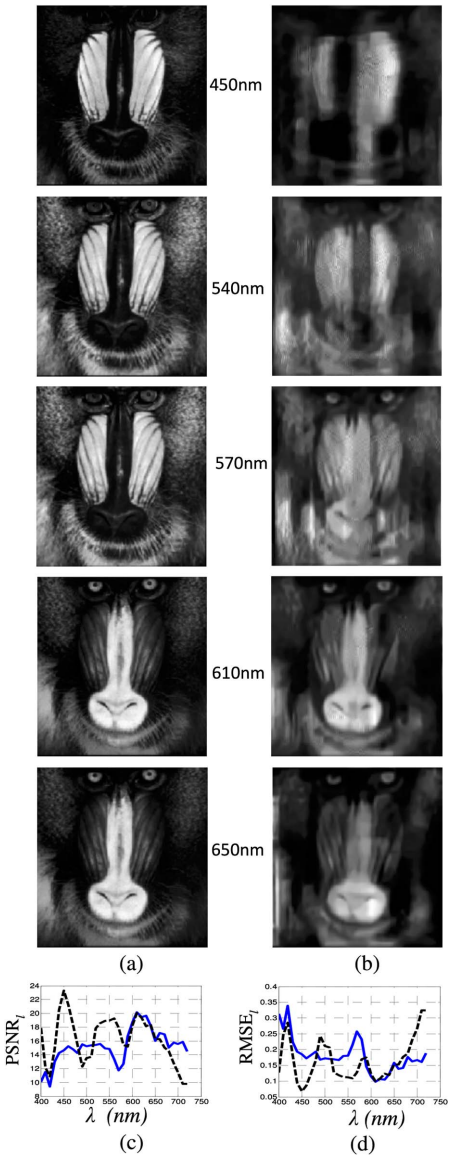

Fig. 10. Five out of 33 monochromatic "mandrill" images extracted from the spectral cubes at wavelengths 450, 540, 570, 610, 650 nm: (a) reference measured with spectral filters; (b) filtered reconstructed images after 20 split Bregman iterations, PSNR_l (RMSE_l in brackets) = 14.64 (0.19), 14.97 (0.18), 11.82 (0.26), 20.15 (0.098), 16.03 (0.16); (c) and (d) PSNR_l and RMSE_l values as functions of wavelength for the filtered monochromatic images that were CS reconstructed from experimental DD image (blue) and from computer-simulated DD image (dashed black).

and black curves relative to reference red curves, decreased from 0.35 to 0.22, 0.21 to 0.13, 0.30 to 0.15, 0.22 to 0.12, 0.30 to 0.10, 0.23 to 0.07, 0.23 to 0.10, and 0.39 to 0.16 at the respective eight spatial sampling points. Based on the feasibility proof provided here, we believe that further developments may lead to improved reconstruction of spectral cubes.

Figure 12 shows RGB images calculated from different spectral cubes of the "peppers" object. Figure 12(a) shows the original object displayed on the iPad screen, Fig. 12(b) shows the RGB image calculated from direct measurements with

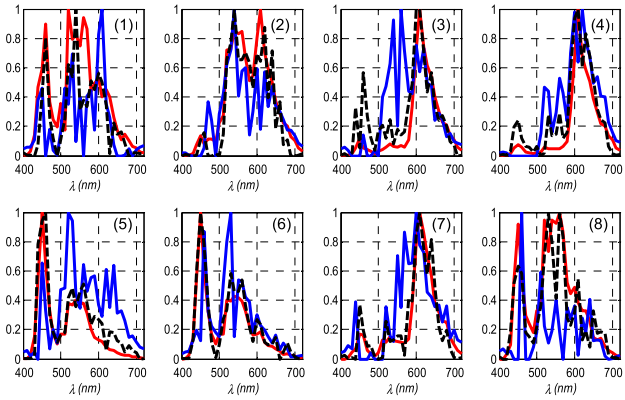

Fig. 11. Normalized intensity for nonfiltered spectra at chosen pixels of reference (red), CS reconstructed from experimental DD image (blue) and from computer-simulated DD image (dashed black) of the "mandrill" with the 33 spectral bands in a range of 400–720 nm. Position of pixels as in Fig. 9(a).

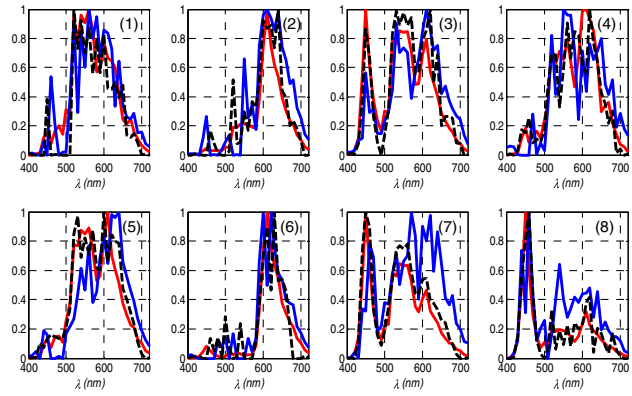

Fig. 13. Normalized intensity for nonfiltered spectra at chosen pixels of reference (red), CS reconstructed from experimental DD image (blue) and from computer-simulated DD image (dashed black) of the "peppers" with the 33 spectral bands in a range of 400–720 nm. Position of pixels as in Fig. 12(a).

33 spectral filters, and Fig. 12(c) shows the DD image recorded at the image sensor with integration time 12.8 ms. Figure 12(d) shows the RGB image built from the spectral cube reconstructed with SBI, Fig. 12(e) shows the RGB image calculated from the noise-filtered reconstructed spectral cube. This RGB image demonstrates substantial improvement in visual quality versus the image in Fig. 12(d). To reemphasize, the RGB image was obtained with a monochromatic image sensor. Finally, Fig. 13 shows nonfiltered spectra at eight spatial sampling points, marked by numbers in Fig. 12(a). The dashed black curves in Fig. 13 show the computer-simulated spectra, which are better fitted to the reference spectra (red lines) than spectra reconstructed from the optical experiment (blue lines). Specifically, the RMSE errors of the blue and black curves, relative to reference red curves, decreased from 0.18 to 0.15, 0.20 to 0.13, 0.20 to 0.13, 0.23 to 0.16, 0.23 to 0.12, 0.14 to 0.13, 0.30 to 0.10, and 0.21 to 0.11 at the respective eight spatial sampling points.

Figure 14 shows RGB images calculated from different spectral cubes of the "color checker" object. Figure 14(a) shows the original object displayed on the iPad screen, Fig. 14(b) shows the RGB image calculated from direct measurements with 33 spectral filters. Figure 14(c) shows the DD image recorded at the image sensor with 12.8 ms integration time. Figure 14(d) shows the RGB image built from the spectral cube reconstructed with SBI. Figure 14(e) shows RGB image calculated from the noise-filtered reconstructed spectral cube, demonstrating substantial improvement in visual quality compared to the image in Fig. 14(d). Finally, Fig. 15 shows nonfiltered spectra at

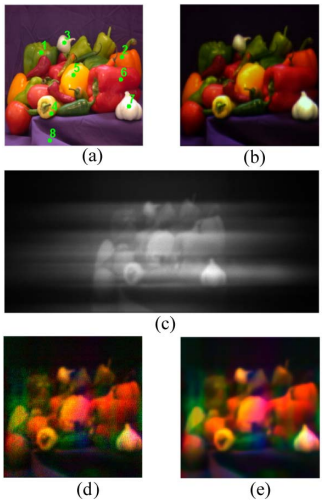

Fig. 12. Object "peppers" with the 33 spectral bands in a range of 400–720 nm: (a) object, (b) reference directly measured with 33 spectral filters and converted to the RGB, (c) dispersed and diffused image optically recorded at the image sensor, (d) reconstructed with CS SI approach and converted to RGB format, (e) noise-filtered after reconstruction before converting to RGB.

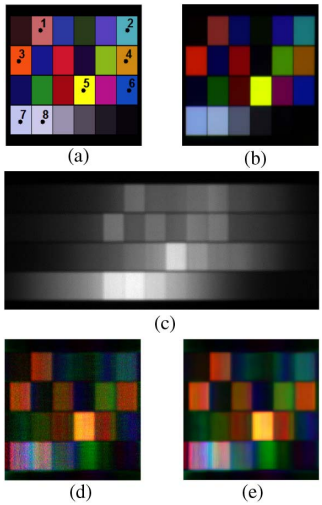

Fig. 14. Object "color checker" with the 33 spectral bands in a range of 400–720 nm: (a) object, (b) reference directly measured with 33 spectral filters and converted to the RGB, (c) dispersed and diffused image optically recorded at the image sensor, (d) reconstructed with CS SI approach and converted to RGB format, (e) noise-filtered after reconstruction before converting to RGB.

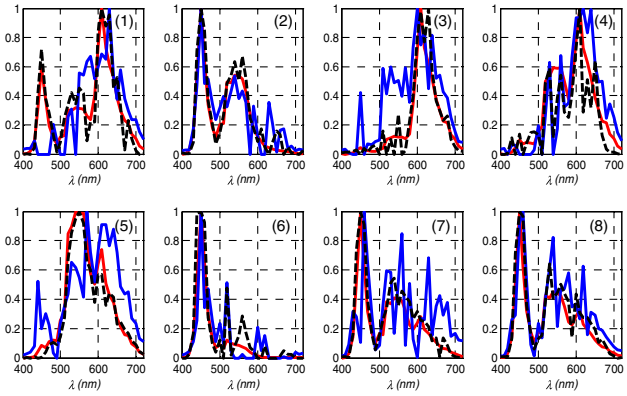

Fig. 15. Normalized intensity for nonfiltered spectra at chosen pixels of reference (red), CS reconstructed from experimental DD image (blue) and from computer-simulated DD image (dashed black) of the "color checker" with the 33 spectral bands in a range of 400–720 nm. Position of pixels as in Fig. 14(a).

eight spatial sampling points, marked by numbers in Fig. 14(a). A comparison between the reference and reconstructed (blue lines) spectra for 33 spectral bands shows again that critical parts of the spectra were satisfactorily captured by our SSI camera and digitally reconstructed. The dashed black curves in Fig. 15 show the computer-simulated spectra, which are better fitted to the reference spectra (red lines) than spectra reconstructed from the optical experiment (blue lines). Specifically, the RMSE errors of the blue and black curves, relative to reference red curves, decreased from 0.22 to 0.11, 0.12 to 0.07, 0.25 to 0.09, 0.20 to 0.16, 0.27 to 0.07, 0.12 to 0.12, 0.27 to 0.09, and 0.17 to 0.10, at the respective eight spatial sampling points. In conclusion, the combination of the RIP diffuser and CS-based algorithms for digital processing worked quite well in snapshot spectral imaging of several test objects.

6. DISCUSSION AND CONCLUSIONS

We showed experimentally the feasibility of snapshot spectral imaging with a regular digital camera complemented by a minor hardware addition in the form of a single phase-only static diffuser. Our architecture, which removes the need for intermediate image plane optics and/or spatial light modulators as well as eliminates lossy amplitude-based modulation by a coded aperture (as in CASSI), can lead to real miniaturization of SSI cameras, therefore providing significant advantages in applications where weight, volume, and/or price are critical. In effect, a miniaturized efficient SI camera may now be considered to be a small sensor rather than a costly system.

The key element of our optical system is a RIP diffuser designed to create a randomized sensing matrix built from calibration measurements of the PSF. The use of a monochromatic sensor instead of a regular mosaic color sensor increases the amount of the captured light and therefore the sensitivity of the camera. Successful acquisition of RGB images by a fully monochromatic image sensor is another important result.

Our method relies substantially on spatial and spectral mixing at the image sensor and subsequent reconstruction of the spectral cube with CS-based algorithms. These prove their ability to reconstruct both spectral and spatial data from spatial-only data acquired by a monochromatic image sensor. This is achieved by proper use of the sparsity property, naturally attributed to photographic images. Large amounts of spectral data are implicitly compressed by combined use of an optical system with a RIP diffuser and of CS-based reconstruction algorithms for spectral imaging. We believe that one of the major advantages in our reported development is the resorting to specific mathematical frame transforms for efficient conversion of the spectral cube into its sparse representation.

Results of this work may have applications in miniaturized snapshot spectral imagers of dynamic objects in such fields as biology, environmental studies, agriculture, food and drug inspection, automotive and vehicle sensors, medical diagnostics, photographic and video cameras, smartphones, wearable devices, augmented reality, remote sensing, and astronomy.

Funding. Ministry of Science, Technology and Space, Israel (3-10416).

Acknowledgment. The authors acknowledge Mr. Omer Inbar for assisting in the performance of certain experiments.

REFERENCES

1. D. J. Brady, *Optical Imaging and Spectroscopy* (Wiley, 2009).
2. Y. Garini, I. T. Young, and G. McNamara, "Spectral imaging: principles and applications," Cytometry Part A **69A**, 735–747 (2006).
3. J. W. Uhr, M. L. Huebschman, E. P. Frenkel, N. L. Lane, R. Ashfaq, H. Liu, D. R. Rana, L. Cheng, A. T. Lin, G. A. Hughes, X. J. Zhang, and H. R. Garner, "Molecular profiling of individual tumor cells by hyperspectral microscopic imaging," Transl. Res. **159**, 366–375 (2012).
4. N. Bedard, R. Schwarz, A. Hu, V. Bhattar, J. Howe, M. Williams, A. Gillenwater, R. Richards-Kortum, and T. Tkaczyk, "Multimodal snapshot spectral imaging for oral cancer diagnostics: a pilot study," Biomed. Opt. Express **4**, 938–949 (2013).
5. V. Zheludev, I. Pölönen, N. Neittaanmäki-Perttu, A. Averbuch, P. Neittaanmäki, M. Grönroos, and H. Saari, "Delineation of malignant skin tumors by hyperspectral imaging using diffusion maps dimensionality reduction," Biomed. Signal Process. Control **16**, 48–60 (2015).
6. R. L. Long, K. B. Walsh, and C. V. Greensill, "Sugar imaging of fruit using a low cost charge-coupled device camera," J. Near Infrared Spectrosc. **13**, 177–186 (2005).
7. D. Lorrente, N. Aleixos, J. Gomez-Sanchis, S. Cubero, O. L. Garcia-Navarrete, and J. Blasco, "Recent advances and applications of hyperspectral imaging for fruit and vegetable quality assessment," Food Bioprocess Technol. **5**, 1121–1142 (2012).
8. H. Lang, "Advances in multispectral and hyperspectral imaging for archaeology and art conservation," Appl. Phys. **106**, 309–323 (2012).
9. D. H. Foster, K. Amano, S. M. C. Nascimento, and M. J. Foster, "Frequency of metamerism in natural scenes," J. Opt. Soc. Am. A **23**, 2359–2372 (2006).
10. G. Themelis, J. Yoo, and V. Ntziachristos, "Multispectral imaging using multiple-bandpass filters," Opt. Lett. **33**, 1023–1025 (2008).
11. M. F. Carlsohn, "Spectral image processing in real-time," J. Real Time Image Process. **1**, 25–32 (2006).
12. M. A. López-Álvarez, J. Hernández-Andrés, and J. Romero, "Developing an optimum computer-designed multispectral system comprising a monochrome CCD camera and a liquid-crystal tunable filter," Appl. Opt. **47**, 4381–4390 (2008).
13. D. L. Donoho, "Compressed sensing," IEEE Trans. Inf. Theory **52**, 1289–1306 (2006).
14. A. Z. Averbuch, P. Neittaanmaki, and V. A. Zheludev, *Spline and Spline Wavelet Methods with Applications to Signal and Image Processing*, Vol. **1** of Periodic Splines (Springer, 2014).

15. E. J. Candès, J. K. Romberg, and T. Tao, "Stable signal recovery from incomplete and inaccurate measurements," Commun. Pure Appl. Math. **59**, 1207–1223 (2006).
16. H. F. Rueda, A. Parada, and H. Arguello, "Spectral resolution enhancement of hyperspectral imagery by a multiple-aperture compressive optical imaging system," Ingeniería e Investigación **34**, 50–55 (2014).
17. C. H. F. Rueda and H. A. Fuentes, "Spatial super-resolution in coded aperture based optical compressive hyperspectral imaging systems," Rev. Fac. Ing. Univ. Antioquia **67**, 7–18 (2013).
18. P. Xie, J. Yang, B. Xue, H. Wang, and Y. Song, "Light flow model of coded aperture snapshot spectral imager," Proc. SPIE **9298**, 92980C (2014).
19. H. Arguello and G. R. Arce, "Restricted isometry property in coded aperture compressive spectral imaging," in *IEEE Statistical Signal Processing Workshop (SSP)* (IEEE, 2012).
20. C. V. Correa, H. Arguello, and G. R. Arce, "Block-based reconstructions for compressive spectral imaging," Proc. SPIE **8717**, 87170F (2013).
21. A. Rajwade, D. Kittle, T.-H. Tsai, D. Brady, and L. Carin, "Coded hyperspectral imaging and blind compressive sensing," SIAM J. Imaging Sci. **6**, 782–812 (2013).
22. C. H. F. Rueda, G. A. R. Calderón, and H. A. Fuentes, "Spectral selectivity in compressive spectral imaging based on grayscale coded apertures," in *XVIII Symposium of Image, Signal Processing, and Artificial Vision* (IEEE, 2013).
23. H. Arguello and G. R. Arce, "Colored coded aperture design by concentration of measure in compressive spectral imaging," IEEE Trans. Image Process. **23**, 1896–1908 (2014).
24. C. V. Correa, H. Arguello, and G. R. Arce, "Compressive spectral imaging with colored-patterned detectors," in *IEEE International Conference on Acoustics, Speech and Signal Processing 2014 (ICASSP)* (IEEE, 2014), pp. 7789–7793.
25. X. Yuan, T. H. Tsai, R. Zhu, P. Llull, D. Brady, and L. Carin, "Compressive hyperspectral imaging with side information," IEEE J. Sel. Top. Signal Process. **9**, 964–976 (2015).
26. A. Stern, Y. Rivenson, and B. Javidi, "Optically compressed image sensing using random aperture coding," Proc. SPIE **6975**, 69750D (2008).
27. R. M. Willet, R. F. Marcia, and J. M. Nichols, "Compressed sensing for practical optical imaging systems: a tutorial," Opt. Eng. **50**, 072601 (2011).
28. A. Wagadarikar, R. John, R. Willett, and D. Brady, "Single disperser design for coded aperture snapshot spectral imaging," Appl. Opt. **47**, B44–B51 (2008).
29. D. Kittle, K. Choi, A. Wagadarikar, and D. Brady, "Multiframe image estimation for coded aperture snapshot spectral imagers," Appl. Opt. **49**, 6824–6833 (2010).
30. H. Arguello and G. Arce, "Code aperture optimization for spectrally agile compressive imaging," J. Opt. Soc. Am. A **28**, 2400–2413 (2011).
31. X. Lin, G. Wetzstein, Y. Liu, and Q. Dai, "Dual-coded compressive hyperspectral imaging," Opt. Lett. **39**, 2044–2047 (2014).
32. L. Wang, Z. Xiong, D. Gao, G. Shi, and F. Wu, "Dual-camera design for coded aperture snapshot spectral imaging," Appl. Opt. **54**, 848–858 (2015).
33. H. Rueda, D. Lau, and G. Arce, "Multi-spectral compressive snapshot imaging using RGB image sensors," Opt. Express **23**, 12207–12221 (2015).
34. Y. Wu, I. Mirza, G. Arce, and D. Prather, "Development of a digital-micromirror-device-based multishot snapshot spectral imaging system," Opt. Lett. **36**, 2692–2694 (2011).
35. L. Gao, R. Kester, N. Hagen, and T. Tkaczyk, "Snapshot image mapping spectrometer (IMS) with high sampling density for hyperspectral microscopy," Opt. Express **18**, 14330–14344 (2010).
36. Q. Zhang, R. Plemmons, D. Kittle, D. Brady, and S. Prasad, "Joint segmentation and reconstruction of hyperspectral data with compressed measurements," Appl. Opt. **50**, 4417–4435 (2011).
37. C. Li, T. Sun, K. Kelly, and Y. Zhang, "A compressive sensing and unmixing scheme for hyperspectral data," IEEE Trans. Image Process. **3**, 1200–1210 (2012).
38. H. Arguello, C. V. Correa, and G. R. Arce, "Fast lapped block reconstructions in compressive spectral imaging," Appl. Opt. **52**, D32–D45 (2013).
39. Y. August, C. Vachman, Y. Rivenson, and A. Stern, "Compressive spectral imaging by random separable projections in both the spatial and the spectral domains," Appl. Opt. **52**, D46–D54 (2013).
40. M. Descour and E. L. Dereniak, "Computed-tomography imaging spectrometer: experimental calibration and reconstruction results," Appl. Opt. **34**, 4817–4826 (1995).
41. J. M. Mooney, V. E. Vickers, M. An, and A. K. Brodzik, "High-throughput hyperspectral infrared camera," J. Opt. Soc. Am. A **14**, 2951–2961 (1997).
42. W. R. Johnson, D. W. Wilson, and G. Bearman, "Spatial spectral modulating snapshot hyperspectral imager," Appl. Opt. **45**, 1898–1908 (2006).
43. N. Hagen and E. L. Dereniak, "Analysis of computed tomographic imaging spectrometers. I. Spatial and spectral resolution," Appl. Opt. **47**, F85–F95 (2008).
44. A. Gorman, D. W. Fletcher-Holmes, and A. R. Harvey, "Generalization of the Lyot filter and its application to snapshot spectral imaging," Opt. Express **18**, 5602–5608 (2010).
45. M. Kudenov, M. Jungwirth, E. Dereniak, and G. Gerhart, "White-light Sagnac interferometer for snapshot multispectral imaging," Appl. Opt. **49**, 4067–4076 (2010).
46. M. A. Golub, M. Nathan, A. Averbuch, E. Lavi, V. A. Zheludev, and A. Schclar, "Spectral multiplexing method for digital snapshot spectral imaging," Appl. Opt. **48**, 1520–1526 (2009).
47. T. Goldstein and S. Osher, "The split Bregman method for l1 regularized problems," SIAM J. Imaging Sci. **2**, 323–343 (2009).
48. J. F. Cai, S. Osher, and Z. Shen, "Split Bregman methods and frame based image restoration," Multiscale Model. Simul. **8**, 337–369 (2010).
49. M. A. Golub, "Generalized conversion from the phase function to the blazed surface-relief profile of diffractive optical elements," J. Opt. Soc. Am. A 1**16**, 1194–1201 (1999).
50. R. G. Baraniuk, M. Davenport, R. A. DeVore, and M. B. Wakin, "A simple proof of the restricted isometry property for random matrices," Constr. Approx. **28**, 253–263 (2008).
51. D. Liang, G. Xu, H. Wang, K. F. King, D. Xu, and L. Ying, "Toeplitz random encoding MR imaging using compressed sensing," in *IEEE International Symposium on Biomedical Imaging: From Nano to Macro* (IEEE, 2009), pp. 270–273.
52. J. F. Cai, S. Osher, and Z. Shen, "Convergence of the linearized Bregman iteration For l_1-norm minimization," Math. Comp. **78**, 2127–2136 (2009).
53. S. Osher, Y. Mao, B. Dong, and W. Yin, "Fast linearized Bregman iteration for compressive sensing and sparse denoising," Math. Sci. **8**, 93–111 (2010).
54. A. Averbuch and V. Zheludev, "Interpolatory frames in signal space," IEEE Trans. Signal Process. **54**, 2126–2139 (2006).
55. Z. Shen, "Wavelet frames and image restorations," in *Proceedings of the International Congress of Mathematicians*, R. Bhatia, ed. (Hindustan Book Agency, 2010), Vol. **IV**, pp. 2834–2863.
56. "Aptina imaging demo kits," http://www.onsemi.com/PowerSolutions/evalBoard.do?id=AGB1N0CS-GEVK (10 July, 2015).
57. D. H. Foster, http://personalpages.manchester.ac.uk/staff/david.foster/Tutorial_HSI2RGB/Tutorial_HSI2RGB.html (28 July, 2015).
58. "Image and video denoising by sparse 3D transform-domain collaborative filtering," http://www.cs.tut.fi/~foi/GCF-BM3D/ (10 November, 2015).